Tidal Resonances in Eccentric White Dwarf Binaries

Ethan McKeever
Phil Arras

This thesis is submitted in partial completion of the requirements of the BS Astronomy-Physics Major

Abstract

Tidal effects play a significant role in the orbital evolution of compact white dwarf binaries and these effects change significantly with eccentric orbits. I calculate the tidal responses and orbital evolution in close eccentric white dwarf binaries inspiraling due to gravitational wave emission. We find that in a constant time lag model that white dwarf spin rates approach a pseudosynchronous spin rate, that tidal heating rates have a clear shape depending on the eccentricity and spin rates of the white dwarfs, and that the frequency evolution index increases significantly near merger due to tidal effects. In a g-mode tidal model, I calculate the tidal response in specific models of Helium and Carbon-Oxygen white dwarfs. I show clear resonances in the white dwarf spin rate and tidal heating levels.

I. INTRODUCTION

In this work I will consider tidal interactions in detached white dwarf binaries inspiraling due to angular momentum and energy loss from emission of gravitational waves. I will consider two tidal models in this work: that of a constant time lag using equations from Hut 1980 [1] and one consisting of a sum over stellar g-modes as can be found in [2].

This work is relevant in the context of broadening our understanding of eccentric binary white dwarfs to accomplish two main goals: binary system identification with LISA data and probing our understanding of white dwarfs. We expect LISA to observe millions of stellar binary systems with many thousand being resolvable [3]. In dense stellar systems like those in the centers of galaxies, we expect to see many binary systems with histories of interactions with other stars which could lead to a high population of eccentric binaries [4]. It is important to have waveforms for these eccentric binary systems ready to aid in data analysis when LISA launches to help distinguish as many sources as possible. Specific eccentric models are needed to match to observation with eccentricities greater than $e \approx 0.2$ [4]. Work is currently being done to develop waveforms for eccentric WD binaries [5] and this work aims to help build the understanding of these systems to aid in producing these waveforms. Eccentric binary waveforms can be used to gather information on the interiors of compact objects [6]. For white dwarf research, this can help us determine interior composition and structure.

This work is organized as follows. Section 2 will motivate the rest of this paper through a review of the observational significance of this work. Section 3 will be a consideration of a tidal model involving constant time lag. Section 4 will include the work on a tidal model of stellar g-modes.

II. OBSERVATIONS AND LISA

This work is motivated by the planned 2037 launch of LISA. This launch will allow us to observe gravitational wave sources at lower frequencies and gravitational wave strain than those currently observable by current ground based detectors. This section will be a review of the LISA engineering as well as a brief section on white dwarf binaries.
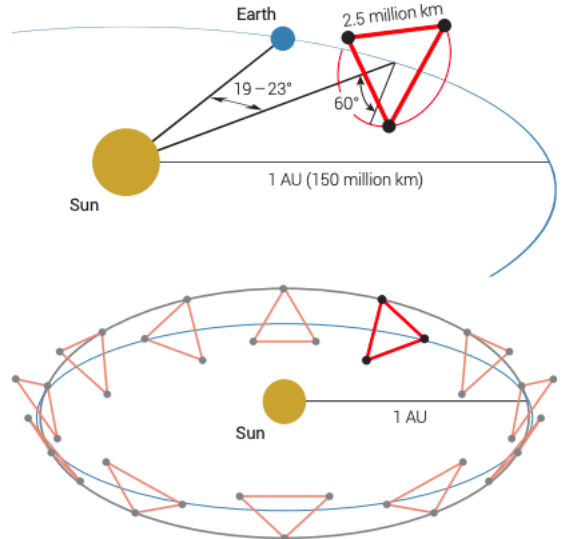

FIG. 1. This image (credit LISA Consortium) shows the orbital overview of the LISA constellation – three spacecraft forming a roughly equilateral triangle with sides of about 2.5 million km.

The general design of LISA is shown in Fig. 1 and Fig. 2 [3]. Fig. 1 shows the overall orbital model and Fig. 2 shows a conceptual mockup of each spacecraft. The spacecraft are arranged to measure the change in distance between test masses in each science arm of the constellation, a total of 6 test masses. This is done through a combination of local interferometers to accurately determine the position of each test mass within the spacecraft and lasers beamed between the spacecraft. Due to the large separation, it is not possible to reflect the lasers between the spacecraft. The telescopes in each arm collect the signal from the opposing lasers, this signal is then sent to the optical bench through an optical fiber cable and a fresh signal is sent out. The received and transmitted light pass through the same aperture. This signal is phase-locked to the initial signal with a fixed offset frequency. To limit back-scattering of the transmitted light from interfering with the received signal an off axis design with 6 curved reflectors requiring a surface figure accuracy of about 30 nm. Each optical bench consists of a "science" interferometer which beams sig-
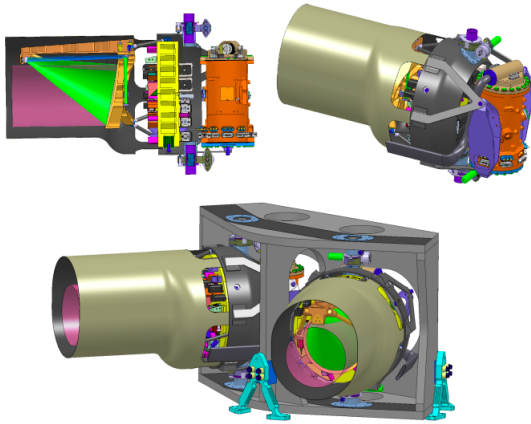
FIG. 2. This image (credit LISA Consortium) shows a conceptual mockup of the scientific equipment of one of the spacecraft in the constellation. It features two identical arms which each include a roughly 30 cm diameter telescope, an optical bench, and a Gravitational Reference Sensor (GRS). All three spacecraft are identical. [3]

FIG. 3. This image (credit LISA Consortium) shows a detailed diagram of the GRS.

nals between spacecraft, a local interferometer to measure the position of the test mass, and a reference interferometer which uses fractions of the two local beams to make beat signals to measure the changes in light travel time between the spacecraft. These optical benches are made out of low-expansion glass-ceramic material to limit path length differences due to temperature variations in the spacecraft. Optical benches with the required alignment precision and stability in orbit were demonstrated in LISA Pathfinder [3] [7]. The optical benches use Differential Wavefront Sensing (DWS), as was demonstrated with LIGO [8], to measure the angles between the interfering wavefronts. This allows for pitch and yaw measurements of the spacecraft relative to their test masses and between the spacecraft. This data is sent to the Drag-Free Attitude Control System (DFACS) which uses cold gas tanks (discussed at the end of this section) to correct for undesired movement of the spacecraft. An Electro-Optic Modulator imprints occasional weak modulations on the transmitted light which allows for transmission of clock noise, time synchronization, and measurement of the absolute distance between spacecraft. This allows an actuator to vary the time dependent point-ahead angle which is required due to the point ahead angle of about eight seconds [3]. The observational data is beamed to the ground each day by one of the spacecraft. This has been calculated to take less than 7.2 hours each day and the daily contact time with a single ground station can last about 8 hours, allowing for a full data transfer each day with a single ground station. Each spacecraft can maintain an alignment to meet the 7.2 hours per day goal for roughly 3 days. The plan is to rotate through the constellation with each spacecraft transmitting for 3 days at a time and a general repointing of antenna on all spacecraft every nine days.
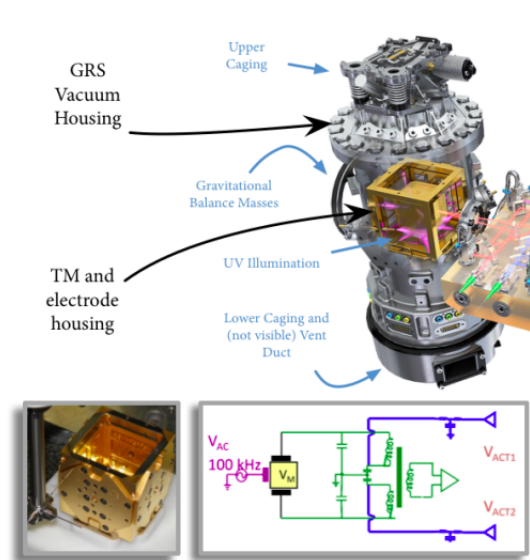
Next we look at the interior design of the GRS. An illustration of the current design is shown in Fig. 3 [3]. The GRS is in a vacuum housing to prevent gas interactions with the test mass. The test mass itself is a roughly 46 mm, 2 kg gold plated gold and platinum cube surrounded by a gold plated electrode housing. These materials are chosen due to low magnetic susceptibility, electrostatic homogeneity, inert surface, and high density. The electrode housing is carefully constructed to allow for 6 degree of freedom rotational and translational capacitive sensing and force/torque application to counteract spurious forces on the test mass. The goal is for the test mass to only be affected by the force of gravity and thus perfectly follow geodesics. Other planned measures to reduce spurious forces include: a 3-4 mm gap between the test mass and electrode housing to reduce gas effects and electrostatic effects, all AC voltage sensing coupled to DC and low frequency electrostatic fields, high thermal conductivity to reduce temperature variations, nearly symmetric geometry around the test mass, and UV LEDs to stimulate photoelectron emission from the test mass or electron housing to balance excess charge from cosmic rays. There are also numerous detection and diagnostic systems in the system to aid in maintaining a low noise level in the test mass movement [3]. A test of the noise level of movement of a single test mass was tested in LISA Pathfinder and is shown compared to the goal level for LISA science goals in Fig. 4 showing that the goal noise level has been demonstrated [9]. LISA pathfinder was launched and was designed specifically to test this test mass noise. A mockup of the core science module for LISA Pathfinder is shown in Fig. 5. The design consisted of two test masses in two gravitational reference sensors connected by an optical bench designed to precisely measure the distance between the two test
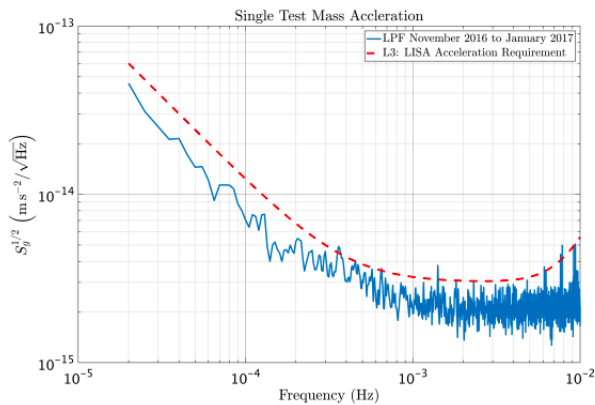
FIG. 4. Noise level for test mass movement from LISA Pathfinder (credit LISA Consortium).

FIG. 6. Conceptual design for each spacecraft showing the cold gas storage and solar panel. The cold gas storage tanks are planned to hold roughly 90 kg of cold gas to allow for a 10-year mission. The solar panel is a 2.9 flat panel and is designed to keep the rest of the spacecraft in shade at all times (credit LISA Consortium).
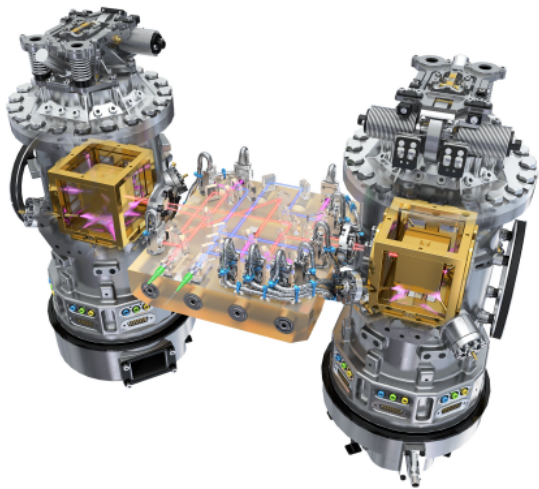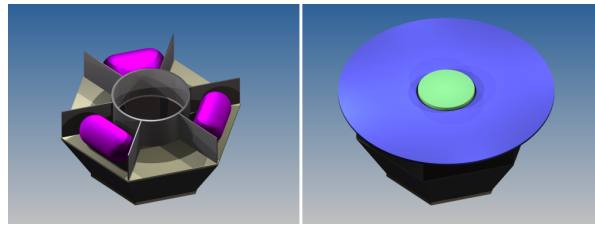

FIG. 5. Conceptual design for the core of LISA Pathfinder designed to measure the distance between two freely floating test masses (credit LISA Consortium).
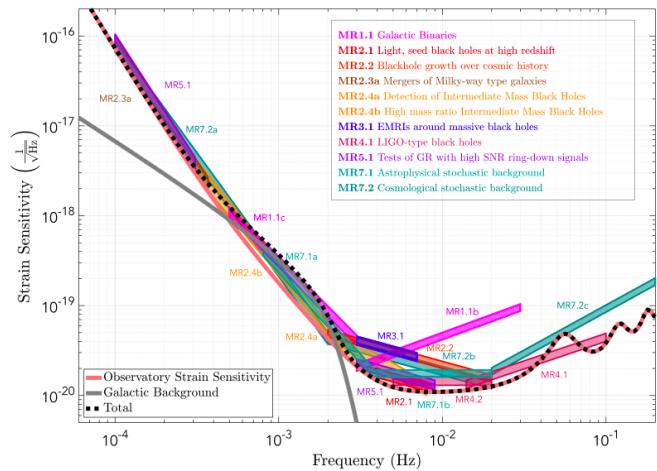

FIG. 7. Mission constraints on a sky-averaged gravitational wave strain sensitivity from an analysis of each observational component and expected strain for different observational sources (credit LISA Consortium).

masses. This gave the data use in Fig. 4 for a single test mass by dividing the LISA Pathfinder noise level by 2 [9].

Next, the spacecraft is designed to shield the test mass from external forces. This is accomplished in two main ways: a large solar panel to keep the rest of the spacecraft in shade to limit temperature fluctuations and to power the electronics and a large cold gas reserve to counteract solar wind effects. A conceptual design of the space-craft is shown in Fig. 6 [3]. The gold gas propulsion system is planned to counteract radiation pressure and other anomalous forces to follow the test masses in their free fall in each interferometric arm. As the test masses are in free fall the spacecraft will be allowed to drift apart from each other. We expect to see relative velocities up to ± 5 m/s and absolute distance changes up to 10,000 km. These distance changes however are quiet at the mHz frequencies that LISA will be observing at and thus won't affect science operations [3].

A detailed look at the expected sensitivity for LISA is shown in Fig. 7 [3]. This figure shows a clear and high frequency dependence on observability of different phenomena. The galactic background strain level is from the very high amount of galactic binaries expected to be observed. There are so many galactic binaries that it is expected that they will be unresolvable at frequencies less than a few mHz and will thus form a 'confusion signal' that will interfere with observations at these frequencies. This has been an important area of research in recent years with LISA mock data challenges being performed to prepare for LISA from a data analysis standpoint and to develop expected signal waveforms. Another impor-tant note is the modulation and increase in the obser-vatory strain sensitivity above roughly 30 mHz. This occurs when the gravitational wave wavelengths become shorter than the arms of the constellation causing partial cancellation of the signal [3].

III. CONSTANT TIME LAG

Here we consider the effects from a tidal model with a constant Time lag as is explored in Hut (1981). This model leads to orbital evolution equations:

$$\dot{a}_{12} = -6\frac{Gmm_2\tau_1k_1}{R_1^3m_1}\left(\frac{R_1}{a}\right)^8\frac{a}{(1-e^2)^{15/2}}$$
$$\times[f_1(e^2)-(1-e^2)^{\frac{3}{2}}f_2(e^2)\frac{\Omega_1}{n}] \quad (1)$$

$$\dot{e}_{12} = -27\frac{Gmm_2\tau_1k_1}{R_1^3m_1}\left(\frac{R_1}{a}\right)^8\frac{e}{(1-e^2)^{13/2}}$$
$$\times[f_3(e^2)-\frac{11}{18}(1-e^2)^{\frac{3}{2}}f_4(e^2)\frac{\Omega_1}{n}] \quad (2)$$

$$\dot{\Omega}_1 = 3\frac{Gm_2^2\tau_1}{R_1^3m_1r_{g_1}^2}\left(\frac{R_1}{a}\right)^6\frac{n}{(1-e^2)^6}$$
$$\times[f_2(e^2)-(1-e^2)^{3/2}f_5(e^2)\frac{\Omega_1}{n}] \quad (3)$$

Here the 12 means the effect on star 1 from star 2. m_1 and m_2 are the stellar masses with $m = m_1 + m_2$. The radius of gyration r_g is defined as $I = M(r_gR)^2$ where I is the moment of inertia and $q_1 = m_1/m_2$ is the mass ratio. τ_1 is the tidal time lag of star 1, k is the tidal love number, e is the eccentricity, Ω_i are the spin rates of each star, n $= (Gm)^{1/2}(a)^{-3/2}$ is the orbital frequency, and the f_i expressions are given as:

$$f_1(e^2) = 1 + \frac{31}{2}e^2 + \frac{255}{8}e^4 + \frac{185}{16}e^6 + \frac{25}{64}e^8 \quad (4)$$

$$f_2(e^2) = 1 + \frac{15}{2}e^2 + \frac{45}{8}e^4 + \frac{20}{64}e^6 \quad (5)$$

$$f_3(e^2) = 1 + \frac{30}{2}e^2 + \frac{15}{8}e^4 + \frac{5}{64}e^6 \quad (6)$$

$$f_4(e^2) = 1 + \frac{3}{2}e^2 + \frac{1}{8}e^4 \quad (7)$$

$$f_5(e^2) = 1 + 3e^2 + \frac{3}{8}e^4 \quad (8)$$

It is easy to get the equations for a_{21} and e_{21}. We then use the effects from the emission of gravitational waves [10]:

$$\dot{a}_{gw} = -\frac{64}{5}\frac{G^3\mu m^2}{c^5a^3}\frac{1}{(1-e^2)^{\frac{7}{2}}}(1+\frac{73}{24}e^2+\frac{37}{96}e^4) \quad (9)$$

$$\dot{e}_{gw} = -\frac{304}{15}\frac{G^3\mu m^2}{c^5a^4}\frac{e}{(1-e^2)^{\frac{5}{2}}}(1+\frac{121}{304}e^2) \quad (10)$$

We can then find the total complete orbital evolution equations for a and e as $\dot{a}(t) = \dot{a}_{12} + \dot{a}_{21} + \dot{a}_{gw}$ and $\dot{e}(t) = \dot{e}_{12} + \dot{e}_{21} + \dot{e}_{gw}$.

With these equations in hand I was able to run orbital simulations in python using the built-in integrator solve_ivp. The simulations were set to evolve based off of time steps, starting at a set initial orbital frequency, eccentricity, and WD spin rates and allowed to evolve until Roche Lobe overflow of either star. To determine the point of Roche Lobe overflow the formula for Roche Lobe radius from Eggleton (1983) was used:

$$r_L = \frac{0.49q^{2/3}}{0.6q^{2/3}+ln(1+q^{1/3})} \quad (11)$$

Three cases of interest were chosen to explore: the ratio of the WD spin rates and the orbital frequency, the tidal heating rate, and the GR frequency evolution power-law index. As is discussed in [10], we can write the frequency evolution as $\dot{f} = \alpha f^\beta$. Then we can plot the index $f\ddot{f}/\dot{f}^2 = \beta$ to find the power law relation. For circular orbits and with no tidal effects we expect an exact value of $\beta = 11/3$. To calculate the tidal heating rate we use the equation from Hut (1981) [1]. This gives the heating luminosity of star 1 as:

$$L_1 = 3\frac{k_1}{T_1}\frac{m_2^2}{m_1}\frac{R_1^8}{a^6}\frac{n^2}{(1-e^2)^{15/2}}[A-2Bx_1+Cx_1^2] \quad (12)$$

Where:

$$T_1 = \frac{R_1^3}{Gm_1\tau_1} \quad (13)$$

$$x_1 = \frac{\Omega_1}{n}(1-e^2)^{3/2} \quad (14)$$

$$A = 1 + \frac{31}{2}e^2 + \frac{255}{8}e^4 + \frac{185}{16}e^6 + \frac{25}{64}e^8 \quad (15)$$

$$B = 1 + \frac{15}{2}e^2 + \frac{45}{8}e^4 + \frac{5}{16}e^6 \quad (16)$$

$$C = 1 + 3e^2 + \frac{3}{8}e^4 \quad (17)$$

First we begin with the results for the WD spin rates. These can be seen plotted in Fig. 8 and Fig. 9. These plots are parametrized by an initial tidal quality factor defined as $\tau_1 = P(0)/(2\pi Q_0)$ where P(0) is the initial orbital period. The simulations are run for initial tidal quality factors of $10^8, 10^9,$ and $10^{1}0$. This is motivated by observational evidence of the WD binary J0651 [11]. When making the plots shown in this section P(0) was set to 10 hours. An important point to consider when looking at the white dwarf spin rates in this model is when $\dot{\Omega} = 0$. As can be seen in Eqn. 3, $\dot{\Omega}$ scales with
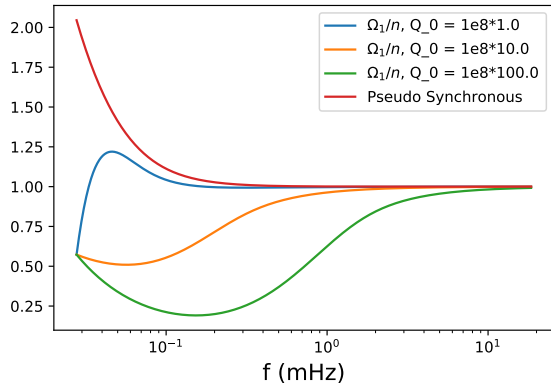
FIG. 8. Ratio of WD spin rates to orbital frequency n for a variety of different tidal quality factors. Both WDs in this simulation are carbon-oxygen white dwarfs with a mass of $0.6 M_\odot$, thus we have only plotted the spin of the first WD as the spins are the same. The initial eccentricity is set to 0.4.

FIG. 10. Tidal heating rates for two white dwarfs for a variety of different tidal quality factors. The first white dwarf has a mass of 0.2 solar masses **vl: use $M_\odot$ for solar mass** and the second a mass of 1.0 solar masses. The initial eccentricity is set to 0.8. The initial WD spin rates are set to 10^{-4}.
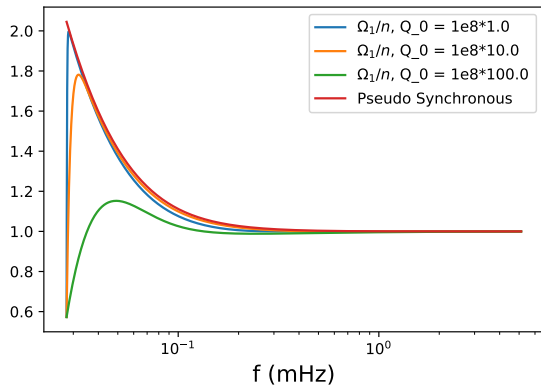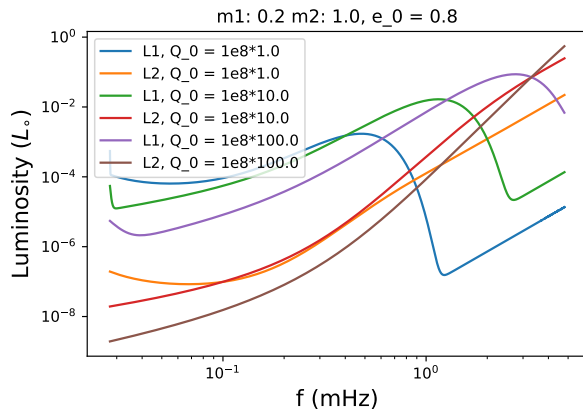

FIG. 9. Ratio of WD spin rates to orbital frequency n for a variety of different tidal quality factors. Both WDs in this simulation are Helium white dwarfs with a mass of $0.2 M_\odot$, thus we have only plotted the spin of the first WD as the spins are the same. The initial eccentricity is set to 0.4.

Ω – thus we can look for a pseudo-synchronous spin rate such that $\Omega = \Omega_{ps} \Rightarrow \dot{\Omega} = 0$. This gives:

$$\Omega_{ps} = n \frac{f_2(e^2)}{(1-e^2)^{3/2} f_5(e^2)} \qquad (18)$$

This pseudo-synchronous spin rate is plotted on Fig. 8 and Fig. 9 to compare to the WD spin rates. From these two plots one can see that the WD spin rates approach the pseudo synchronous rotation rate. As the eccentricity dies out due to the emission of gravitational waves we see that Ω_{ps} dies out to $n\Omega$, as we expect. Stars with a smaller tidal quality factor grant larger time lags which increases $\dot{\Omega}$ which allows the stars to synchronize faster. The large dependence on stellar radius in $\dot{\Omega}$ allows the lighter helium white dwarfs to synchronize more quickly

than their heavier carbon-oxygen counterparts given the inverse relation between white dwarf mass and radius. This expected behavior is clearly seen when comparing the two plots.

Next we take a look at the tidal heating rate of each white dwarf. An example tidal heating plot is shown in Fig. 10. There are a few important details that can be seen in this plot. First we look back at the tidal heating equations For a small ratio Ω/n we get that x is very small which grants $A - 2Bx + Cx^2 \approx A$. As the WD rapidly spins up we then get $A - 2Bx + Cx^2 \approx A - 2Bx$ so we get a rapid decrease in the heating rate. This is seen more easily in the 0.2 solar mass WD as it is able to spin up faster and thus has a sharper drop in heating during this initial period. This effect is inversely related to the initial tidal quality factor and thus we see sharper drops for smaller initial quality factors. We then see a slow ramp up and then a decrease in heating power around 1 mHz. This is also easily explained by the tidal heating equations earlier in this section. The main effect here is that the tidal heating rate is related to the semi major axis by a factor a^{-6} so as the semi-major axis decreases we see an increase in the heating rate. Then for a WD spinning near the pseudosynchronous frequency, as the eccentricity shrinks, the term $A - 2Bx + Cx^2$ approaches zero. This causes a drop in the tidal heating rate - this can be seen for the 0.2 solar mass WD but not the 1.0 solar mass WD as the former is near pseudosynchronous spin when the eccentricity falls below about 0.2 while the heavier WD is not. The WD spin rate never fully reaches pseudosynchronous spin rate, the spins lag behind by a small margin that depends on the tidal time lag. A greater time lag leads to a higher value for $\dot{\Omega}$ which allows for a spin closer to pseudosynchronous. We see this in Fig. 10 where the lines that have a higher initial tidal quality factor and thus a lower time lag have greater tidal heat-
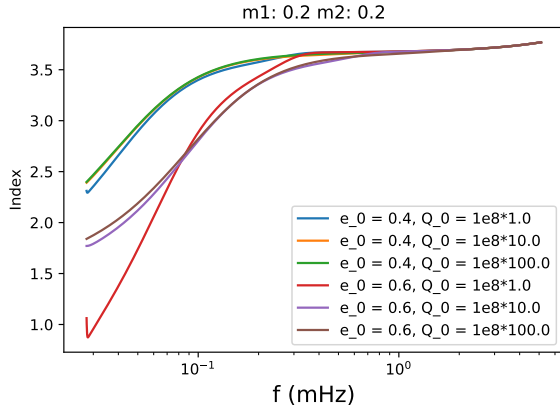
FIG. 11. Frequency evolution index in a system of two 0.2 solar mass white dwarfs under a range of initial conditions. The effects in this plot are dominated by the effects from the emission of gravitational waves and thus we see largely what we expect for a pure GR case.

ing as the spin rate as not as close to pseudosynchonous and thus the term $A - 2Bx + Cx^2$ is larger. This effect is greater than the linear dependence of the heating on the time lag. This is what causes the higher initial quality factor lines to surpass those with lower quality factors at later times.

Once the eccentricity sinks to a low enough level where $A, B, C \approx 1$ and the WD spin has sufficiently neared the pseudosynchronous spin rate then the factor $A - 2Bx + Cx^2$ becomes constant and the only change in the heating rate is from the change in semi-major axis. This leads to the linear line on the plot for the 0.2 solar mass WD models at later times.

Next, we look at the frequency evolution index. An example plot is shown in Fig. 11.

IV. TIDAL RESONANCES

We now consider a different tidal model consisting of a sum over stellar g-modes. Our orbital evolution equations comes from Weinberg et al. (2013) [12]. We get:

$$\dot{a} = -4a\frac{m_j}{m_i}\sum_{a,l,m,k}\left(\frac{R_i}{a}\right)^{2l+1}(W_{lm}I_{alm}X_k^{lm})^2$$

$$\times$$

$$\frac{|\omega_a|k\Omega\gamma_a}{(|\omega_a| - k\Omega)^2 + \gamma_a^2} \quad (19)$$

$$\dot{e} = 2\Omega\left(\frac{1-e^2}{e}\right)\frac{m_j}{m_i}\sum_{a,l,m,k}\left(\frac{R_i}{a}\right)^{2l+1}(W_{lm}I_{alm}X_k^{lm})^2$$

$$\times$$

$$\frac{|\omega_a|k\Omega\gamma_a}{(|\omega_a| - k\Omega)^2 + \gamma_a^2}[-k + \frac{m}{\sqrt{1-e^2}}] \quad (20)$$

$$I_i\dot{\Omega}_i = 4a\frac{Gm_j^2}{R_i}\sum_{a,l,m,k}\left(\frac{R_i}{a}\right)^{2l+2}(W_{lm}I_{alm}X_k^{lm})^2$$

$$\times$$

$$\frac{|\omega_a|m\gamma_a}{(|\omega_a| - k\Omega)^2 + \gamma_a^2} \quad (21)$$

with,

$$W_{lm} = 4\pi\frac{Y_{lm}(\frac{\pi}{2}, 0)}{2l+1} \quad (22)$$

where Y_{lm} are the spherical harmonics. W_{lm} are nonzero only if l-m iz even. In this work we only consider the quadrupolar modes so the only nonvanishing values of W_{lm} are $W_{20} = -\sqrt{\pi/5}$ and $W_{2\pm2} = \sqrt{3\pi/10}$. I_{alm} are the linear overlap integrals and are given by:

$$I_{alm} = \frac{1}{MR^l}\int d^3x\rho\boldsymbol{\xi}_a^* \cdot \nabla(r^l Y_{lm}) \quad (23)$$

The Hansen coefficients X_k^{lm} are used as an expansion of the time-dependence of the Keplerian orbit and are defined as:

$$\left(\frac{a}{D}\right)^{l+1}e^{-im\Phi} = \sum_{k=-\infty}^{\infty}X_k^{lm}(e)e^{-ik\Omega t} \quad (24)$$

Which grants:

$$X_k^{lm}(e) = \frac{\Omega}{2\pi}\int_0^{2\pi/\Omega}dt e^{ik\Omega t - im\Phi}\left(\frac{a}{D}\right)^{l+1} \quad (25)$$

Where D is the orbital separation. It is important to note that the Hansen coefficients are only a function of eccentricity and thus must only be computed once in a simulation for a circular orbit. ω_a are the mode angular frequencies and γ_a are the mode damping rates for the individual g-modes. The sum over a,l,m, and k can be broken down using these components. We are limiting our scope to quadrupolar modes so we fix l=2 and sum over m=-2,0,2 as W_{lm} is vanishing otherwise. Our sum over k is limited by the Hansen coefficients. The Hansen coefficients are only significant for a small number of k near zero. The limiting case of k can be characterized as $k_{crit} = (1-e)^{-1.5}$. For the work here k was summed from the integers nearest $-18 * k_{crit}$ and $22 * k_{crit}$. A plot showing the Hansen coefficients for this range of k for eccentricities of 0.0,0.3,0.6,and 0.9 are shown in Fig. 12 The sum over a is the sum over the g-modes. The g-modes drop out at higher values of a. For this work the first 500 modes were included. The mode values: ω_a, γ_a, and I_{alm} were reconstructed from fits in Table 3 of Burkart et al (2021). Next we note that the modes in [12] are given by:

$$q_a(t) = \sum_k U_a^{(k)}\frac{\omega_a}{\omega_a - k\Omega - i\gamma_a}e^{-ik\Omega t} \quad (26)$$

which gives the rate at which mode energy damps to heat as:

$$\dot{E}_{heat} = 2\sum_{a,l,m,k}\gamma_a|U_a^{(k)}\frac{\omega_a}{\omega_a - k\Omega - i\gamma_a}|^2\left(\frac{GM^2}{R}\right) \quad (27)$$
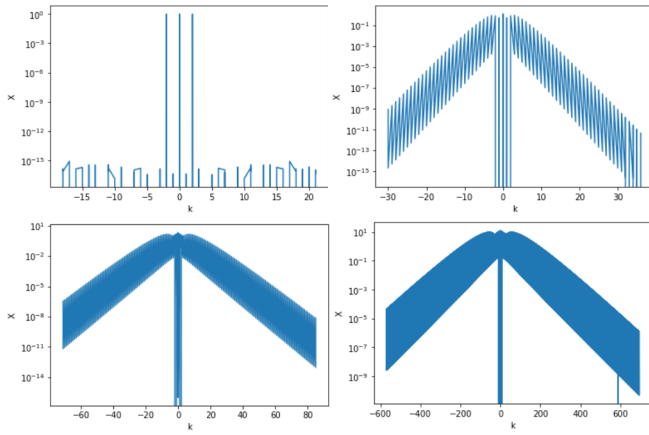
FIG. 12. Hansen coefficient values for eccentricities of 0.0, 0.3, 0.6 and 0.9 in the order: top left, top right, bottom left, bottom right. These values are for k in the range $-18(1 - e)^{-1.5}$ to $22(1 - e)^{-1.5}$ which is what was used in this work. Note that only $k > 0$ with a nonzero Hansen coeffient in the circular case is $k = 2$.

$$\dot{E}_{heat} = \sum_{a,l,m,k} (U_a^{(k)})^2 \frac{2\gamma_a \omega_a^2}{(\omega_a - k\Omega)^2 + \gamma_a^2} \left(\frac{GM^2}{R} \right) \quad (28)$$

With

$$U_a^{(k)} = \frac{m_j}{m_i} \sum_{lm} W_{lm} I_{alm} X_k^{lm}(e) \left(\frac{R}{a} \right)^{l+1} \quad (29)$$

This grants the tidal heating rate which I will discuss a little later.

When running simulations for this tidal model a few issues became apparent. Most of these issues come from the term:

$$\frac{1}{(|\omega_a| - k\Omega)^2 + \gamma_a^2} \quad (30)$$

that appears in the orbital evolution equations. The important note here is that the mode damping rates are many orders of magnitude smaller than the mode frequency and orbital frequency. Thus we get an equilibrium tide that is many orders of magnitude smaller than the resonant tide when $\omega_a \approx k\Omega$ and this factor becomes roughly $1/\gamma_a^2$. In the orbital evolution equations, the tidal term is several orders of magnitude smaller than the gravitational wave term when at equilibrium and then several orders of magnitude larger when at resonance. The built in python integrator solve_ivp struggles with this type of equation. The integrator takes larger and larger steps as the equations behaves as expected. The gravitational wave term follows a clear form and the integrator takes large steps as it is able to predict what the gravitational wave term will look like at higher frequencies. As the integrator takes big time steps it begins to completely miss tidal resonances – the main object of study. Then, if forced to take small time steps and with a low accuracy threshold the runge-kutta integrators in

solve_ivp fail to integrate the resonance and the program quits. Switching the integrator to an LSODA method was able to fix the problem of the code not finishing but there was still the question of how to manipulate the two remaining levers – the error tolerances and setting a maximum step size – to ensure that each resonance is properly accounted for. Here we run into the issue of integration time. Each time step takes on the order of a second as the Hansen coefficients must be computed every time and the sum over a,l,m,k has over 50,000 terms. One can try to set the maximum step size to be thinner than a resonance by solving for the orbital frequencies where the tidal and gravitational wave terms in the expression for $\dot{a}$ for a fixed mode and finding the difference in frequency between these two steps and then using Kepler's third law to convert to a step in a and then using the gravitational wave term to convert to a timestep. Doing this properly grants a small timestep – on the order of $10^3 - -10^4$ which would take years to run. Similarly, trying to get the desired effect by lowering the error tolerances provides no meaningful effect when the error tolerance setting allows the simulation to finish in less than a week. We need to then find a combination of these two effects that gives the desired plot. The goal here is to find a plot that looks correct and has all of the resonances that we want and that doesn't change when we significantly improve the accuracy of the simulation beyond that point. First, we need to consider what "looks" correct. One important diagnostic tool is that noted in Fig. 12. The only $k > 0$ where the Hansen coefficient is nonzero is $k = 2$ from the term $|\omega_a| - k\Omega$ in Eqn. 26 we see that to have a resonance we need a positive k and so we see that the only term that can have a resonance in a circular orbit is the term with k=0 so $|\omega_a| = 2\Omega$. This means we can look at the mode frequencies and predict exactly where we will see resonances. As the height of the resonance is almost entirely determined by the mode damping frequencies which are similar for modes with frequencies that are close to each other we expect each resonance to be a similar size (in the circular case), thus we just need to make circular orbital simulations and pay attention to the behavior of the resonances. Fig. 13 shows the difference between an incorrect plot and a correct one. It was found that setting the absolute and relative error tolerances to 10^{-8} and the maximum step size to 10^{10} gave the desired plots. Now, with this in hand we can analyze plots and compare them to those in Section III. We begin by looking at the spin rate of the white dwarfs. The circular case can be seen in Fig. 13. An eccentric case is shown in Fig. 14. This shows an example of two WDs spinning up from zero initial spin with an initial eccentricity of 0.4. At higher eccentricities we have more values of k with significant Hansen coefficients and so we expect more resonances. As the eccentricity dies out, so do these higher Hansen coefficients and we expect less resonances. We see this exact behavior in Fig. 14. We see lots of smaller steps in between the main resonances we can see in both figures and then as the eccentricity
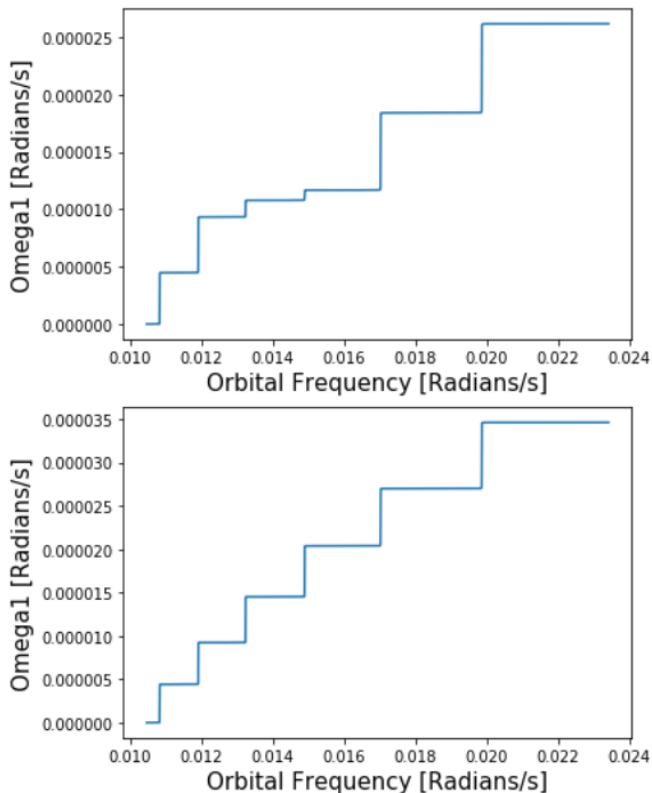
FIG. 13. White Dwarf spin rate vs. orbital spin rate in the circular case. These plots show the difference between a code that correctly accounts for resonances vs one that doesn't.
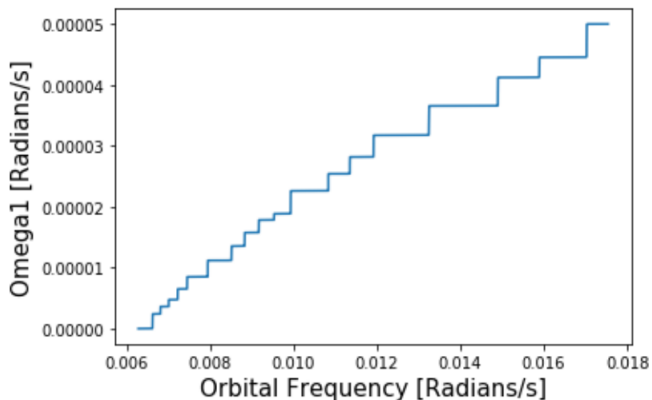

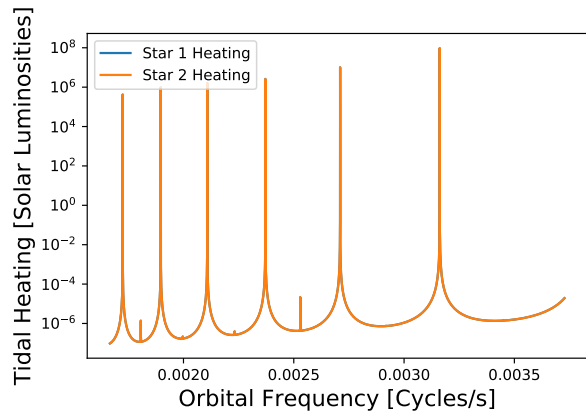FIG. 14. WD spin rates for two identical 0.2 solar mass WD models.

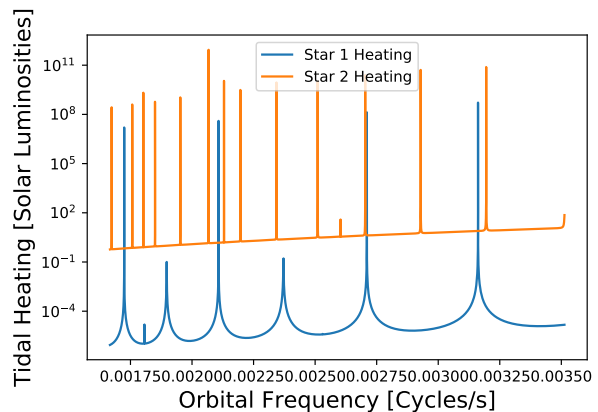FIG. 15. WD heating for a circular orbit with a system of two identical 0.2 solar mass Helium WDs.

FIG. 16. WD heating for a circular orbit. Star 1 is a 0.2 solar mass helium WD and star 2 is a 0.6 solar mass carbon-oxygen WD.

dies out over the frequency space we see less and less of these smaller steps in WD spin rate.

Next, we look at the WD heating rate given in Eqn. 28. An example heating plot for 2 0.2 solar mass WDs in a circular orbit is shown in Fig. 15. Here we can see the resonances that we expect to see from the resonance term in the heating equations. As this is a circular orbit, it is easy to check that the resonances are exactly where we expect them to be. We can see an equilibrium heating term of about 10^{-6} solar luminosities for each WD and resonant heating terms of 10^6-10^8 solar luminosities. We can also see some small spikes in between the resonances. It is believed that these are unphysical and are the result of some failing of the integrator. There is nothing in the equations that would predict small increases like this for a circular orbit. Next we want to look at what the heating rates look like for a system of two different WD models. Here we look at a binary of one 0.6 solar mass carbon-oxygen WD and one 0.2 solar mass Helium WD. This is shown in Fig. 16 There are a few important things to note in this plot. First we see that the equilibirum heating rate for the carbon-oxygen WD is much higher and exceeds a solar luminosity at higher frequencies. This plot also correctly hits all of the resonances that we expect in a circular orbit for a carbon-oxygen WD. The concern that can be seen in Fig. 15 reappears here – there are anomalous spikes in heating that appear to be unphysical and have no width. Due to the thinner width on the carbon-oxygen resonances it can be hard

to tell that two of the spikes at lower frequencies are of this nature. One right aboe the first anomalous spike in WD 1 and one immediately to the right of the first WD 1 resonance after 0.002 Hz. We should also note that the resonances are much thinner for the carbon oxygen WD than for the helium WD. This is due to the much higher equilibrium heating term so that the resonant term of any single mode must be much closer to resonance to dominate. The resonances for the carbon-oxygen WD are also smaller as the damping rate for the carbon-oxygen WD is larger. At the modes seen here the mode damping rates for the carbon-oxygen WD are roughly 2 orders of magnitude larger than the ones for the helium WD model. Finally we note that a couple of the resonances for the helium WD are smaller than expected. This is probably due to an integration error as the integrator struggles with two different WD models. These simulations will be retested again with stricter error tolerances to test this hypothesis.

When looking at the heating plots Fig. 15 and 16, one notices the significant heights of the heating peaks. We want to compare these to the Eddington Limit. The Eddington Luminosity is given by:

$$L_{edd} = \frac{4\pi GM m_p c}{\sigma_T} \approx 3.2 * 10^4 \left(\frac{M}{M_\circ}\right) L_\circ \qquad (31)$$

We can see in these plots that the heating at resonance exceeds this Eddington Limit, sometimes by many orders of magnitude. These WD models all are made out of atoms with twice the number of nucleons than electrons and so we would need twice the Eddington Luminosity to drive an outflow but this won't make a difference when the tidal heating incites a Luminosity several orders of magnitude above the Eddington Limit. These sharp peaks above the Eddington Luminosity are a breakdown of our linear model near resonance. As the frequency nears the resonant frequency the evolution equations become highly nonlinear and our linear approximation is no longer appropriate. Here I will show a quick demonstration of this effect. We consider a circular orbit of 2 Helium WD models. Then the resonant frequency for a mode is given by $\omega_a = 2\Omega$. We look at the mode away from resonance:

$$|q_a| \approx U_a^{(2)} \frac{\omega_a}{\omega_a - 2\Omega} \qquad (32)$$

Here

$$U_a^{(2)} \approx 3I_a \left(\frac{R}{a}\right)^3 \qquad (33)$$

We consider that the resonance here is given by $\omega_a = 2\Omega$ and define the frequency difference from resonance as $\Delta = \omega_a - 2\Omega$. We then constrain our linear order approximation to be when $|q| \leq 1$. Then we enter the nonlinear regime when $|q| = 1$ or when

$$\Delta \approx 3\omega_a I_a \left(\frac{R}{a}\right)^3 \qquad (34)$$

For mode 10 in the He5 model we have: $\omega_a = 0.024$, $I_a = 9.8 * 10^{-5}$, and at resonance $(R/a)^3 = 0.014$. This grants $\Delta = 9.9 * 10^{-8}$ Radians/s. For this mode the damping rate is given by $\gamma_a = 4.8 * 10^{-15}$. We see a significant resonance spike when $\Delta \approx \gamma_a$ and we see a breakdown of our linear order approximation at a Δ 7 orders of magnitude greater than this. Thus we cannot fully trust our results this close to resonance. This explains these anomalous heating spikes in Fig. 15 and Fig. 16. In further work these nonlinear effects must be accounted for. A discussion of this is available in [2].

V. CONCLUSION

This work presents a number of results for these two different tidal models. It makes predictions for what we will see for the WD spin rate and tidal heating for each model. For the case of constant time lag we also make predictions for the frequency evolution index of the orbit. This is one way we will be able to directly observe the orbital behavior through gravitational waves directly. We also see that we expect significant tidal heating luminosity close to merger for both models and super-Eddington luminosities near resonances in the second model. We see that in the first model the WD spin rates approach a pseudo-synchronous spin rate depending on the eccentricity that falls to the orbital frequency for circular orbits. For the second model we see resonance steps in frequency as the WD spin rates attempt to keep up with the orbital frequency evolution. We do not expect to see the WD spin rates reach the orbital frequency as we did not include "resonance locking" as seen in [2]. In this work so far the mode quantities: ω_a, I_{alm}, and γ_a were taken to be constants of each mode. This approximation falls apart for higher WD spins and there we would need to account for the rotating reference frame effects on these quantities. Further work on this project will include these effects and provide a more accurate model of tidal effects in regimes with highly spinning white dwarfs.

[1] P. Hut, Tidal evolution in close binary systems., Astronomy & Astrophysics **99**, 126 (1981).

[2] J. Burkart, E. Quataert, P. Arras, and N. N. Weinberg, Tidal resonance locks in inspiraling white dwarf binaries,

Monthly Notices of the Royal Astronomical Society **433**, 332 (2013).

[3] P. Amaro-Seoane, H. Audley, S. Babak, J. Baker, E. Barausse, P. Bender, E. Berti, P. Binetruy, M. Born, D. Bortoluzzi, J. Camp, C. Caprini, V. Cardoso, M. Colpi, J. Conklin, N. Cornish, C. Cutler, K. Danzmann, R. Dolesi, L. Ferraioli, V. Ferroni, E. Fitzsimons, J. Gair, L. G. Bote, D. Giardini, F. Gibert, C. Grimani, H. Halloin, G. Heinzel, T. Hertog, M. Hewitson, K. Holley-Bockelmann, D. Hollington, M. Hueller, H. Inchauspe, P. Jetzer, N. Karnesis, C. Killow, A. Klein, B. Klipstein, N. Korsakova, S. L. Larson, J. Livas, I. Lloro, N. Man, D. Mance, J. Martino, I. Mateos, K. McKenzie, S. T. McWilliams, C. Miller, G. Mueller, G. Nardini, G. Nelemans, M. Nofrarias, A. Petiteau, P. Pivato, E. Plagnol, E. Porter, J. Reiche, D. Robertson, N. Robertson, E. Rossi, G. Russano, B. Schutz, A. Sesana, D. Shoemaker, J. Slutsky, C. F. Sopuerta, T. Sumner, N. Tamanini, I. Thorpe, M. Troebs, M. Vallisneri, A. Vecchio, D. Vetrugno, S. Vitale, M. Volonteri, G. Wanner, H. Ward, P. Wass, W. Weber, J. Ziemer, and P. Zweifel, Laser interferometer space antenna (2017), arXiv:1702.00786 [astro-ph.IM].

[4] J. Samsing, M. MacLeod, and E. Ramirez-Ruiz, THE FORMATION OF ECCENTRIC COMPACT BINARY INSPIRALS AND THE ROLE OF GRAVITATIONAL WAVE EMISSION IN BINARY-SINGLE STELLAR ENCOUNTERS, The Astrophysical Journal **784**, 71 (2014).

[5] S. Y. Lau, K. Yagi, and P. Arras, A New Waveform Model for Eccentric Binary White Dwarf Systems, in *APS April Meeting Abstracts*, APS Meeting Abstracts, Vol. 2021 (2021) p. L16.003.

[6] R. Gold, S. Bernuzzi, M. Thierfelder, B. Brügmann, and F. Pretorius, Eccentric binary neutron star mergers, Physical Review D **86**, 10.1103/physrevd.86.121501 (2012).

[7] M. Armano, H. Audley, G. Auger, J. T. Baird, M. Bassan, P. Binetruy, M. Born, D. Bortoluzzi, N. Brandt, M. Caleno, L. Carbone, A. Cavalleri, A. Cesarini, G. Ciani, G. Congedo, A. M. Cruise, K. Danzmann, M. de Deus Silva, R. De Rosa, M. Diaz-Aguiló, L. Di Fiore, I. Diepholz, G. Dixon, R. Dolesi, N. Dunbar, L. Ferraioli, V. Ferroni, W. Fichter, E. D. Fitzsimons, R. Flatscher, M. Freschi, A. F. García Marín, C. García Marirrodriga, R. Gerndt, L. Gesa, F. Gibert, D. Giardini, R. Giusteri, F. Guzmán, A. Grado, C. Grimani, A. Grynagier, J. Grzymisch, I. Harrison, G. Heinzel, M. Hewitson, D. Hollington, D. Hoyland, M. Hueller, H. Inchauspé, O. Jennrich, P. Jet-

zer, U. Johann, B. Johlander, N. Karnesis, B. Kaune, N. Korsakova, C. J. Killow, J. A. Lobo, I. Lloro, L. Liu, J. P. López-Zaragoza, R. Maarschalkerweerd, D. Mance, V. Martín, L. Martin-Polo, J. Martino, F. Martin-Porqueras, S. Madden, I. Mateos, P. W. McNamara, J. Mendes, L. Mendes, A. Monsky, D. Nicolodi, M. Nofrarias, S. Paczkowski, M. Perreur-Lloyd, A. Petiteau, P. Pivato, E. Plagnol, P. Prat, U. Ragnit, B. Raïs, J. Ramos-Castro, J. Reiche, D. I. Robertson, H. Rozemeijer, F. Rivas, G. Russano, J. Sanjuán, P. Sarra, A. Schleicher, D. Shaul, J. Slutsky, C. F. Sopuerta, R. Stanga, F. Steier, T. Sumner, D. Texier, J. I. Thorpe, C. Trenkel, M. Tröbs, H. B. Tu, D. Vetrugno, S. Vitale, V. Wand, G. Wanner, H. Ward, C. Warren, P. J. Wass, D. Wealthy, W. J. Weber, L. Wissel, A. Wittchen, A. Zambotti, C. Zanoni, T. Ziegler, and P. Zweifel, Sub-femto-g free fall for space-based gravitational wave observatories: Lisa pathfinder results, Phys. Rev. Lett. **116**, 231101 (2016).

[8] B. A. et al., Observation of gravitational waves from a binary black hole merger, Physical Review Letters **116**, 10.1103/physrevlett.116.061102 (2016).

[9] M. Armano, H. Audley, J. Baird, P. Binetruy, M. Born, D. Bortoluzzi, E. Castelli, A. Cavalleri, A. Cesarini, M. Cruise, K. Danzmann, M. de Deus Silva, I. Diepholz, G. Dixon, R. Dolesi, L. Ferraioli, V. Ferroni, E. Fitzsimons, M. Freschi, L. Gesa, F. Gibert, D. Giardini, R. Giusteri, C. Grimani, J. Grzymisch, I. Harrison, G. Heinzel, M. Hewitson, D. Hollington, D. Hoyland, M. Hueller, H. Inchauspe, O. Jennrich, P. Jetzer, N. Karnesis, B. Kaune, N. Korsakova, C. J. Killow, A. Lobo, I. Lloro, L. Liu, J.-P. Lopez-Zaragoza, R. Maarschalkerweerd, D. Mance, N. Meshksar, V. Martın, L. Martin-Polo, J. Martino, F. Martin-Porqueras, I. Mateos, P. McNamara, J. Mendes, L. Mendes, M. Nofrarias, S. Paczkowski, M. Perreur-Lloyd, A. Petiteau, P. Pivato, E. Plagnol, J. Ramos-Castro, J. Reiche, D. Robertson, F. Rivas, G. Russano, J. Slutsky, C. Sopuerta, T. Sumner, D. Texier, I. Thorpe, D. Vetrugno, S. Vitale, G. Wanner, H. Ward, P. Wass, W. Weber, L. Wissel, A. Wittchen, and P. Zweifel, Lisa pathfinder (2019), arXiv:1903.08924 [astro-ph.IM].

[10] M. Maggiore, Michele Maggiore: Gravitational waves. Volume 1: theory and experiments. Oxford University Press, 2007, 576p., GBP47.00, ISBN13: 978-0-19-857074-5, General Relativity and Gravitation **41**, 1667 (2009).

[11] A. L. Piro, Tidal Interactions in Merging White Dwarf Binaries, The Astrophysics Journal Letters **740**, L53 (2011), arXiv:1108.3110 [astro-ph.SR].

[12] N. Weinberg, P. Arras, E. Quataert, and J. Burkart, Nonlinear tides in close binary systems, Astrophysical Journal **751** (2011).